Characterization of IMIC, an implantable needle-shaped positron sensitive monolithic active pixel sensor for preclinical molecular neuroimaging

S El Ketara, F Agnese, L Ammour, S Bouvard, O Clausse, M Dupont, F Gensolen, M Goffe, M Kachel, J Laurence, et al.

Characterization of IMIC, an implantable needle-shaped positron sensitive monolithic active pixel sensor for preclinical molecular neuroimaging

S. El ketara[1,2], F. Agnese[3], L. Ammour[4], S. Bouvard[5], O. Clausse[3], M. Dupont[6], F. Gensolen[6], M. Goffe[3], M. Kachel[3], J. Laurence[6], P. Pangaud[6], C. Wabnitz[3], T. Weicherding[6], J. Baudot[3], P. Lanièce[1,2], C. Morel[6], L. Zimmer[5], M.-A. Verdier[1,2]

[1] Université Paris-Saclay, CNRS/IN2P3, IJCLab, 91405 Orsay, France
[2] Université Paris Cité, IJCLab, F-91405, Orsay, France
[3] Université de Strasbourg, CNRS, IPHC UMR 7178, F-67000 Strasbourg, France
[4] Nantes Université, CHU Nantes, F-44000 Nantes, France
[5] Université Claude Bernard Lyon 1, CNRS, INSERM, Hospices Civils de Lyon, CERMEP, Lyon, France
[6] Aix Marseille Univ, CNRS/IN2P3, CPPM, Marseille, France

Abstract

The correlation of molecular neuroimaging and behavior studies in preclinical PET imaging is of major interest to unlock progress in the understanding of brain processes and assess the validity of preclinical studies in drug development. However, fully achieving this ambition requires performing molecular images of awake and freely moving animals, whereas most of the preclinical imaging procedures are currently performed under anesthesia. To overcome this issue, the MAPSSIC project aims to develop a pixelated intracerebral probe to be implanted into awake and freely moving rats. The aforementioned probe relies on IMIC (Imageur Moléculaire Intra Cérébral), a Monolithic Active Pixel Sensor (MAPS) prototype set to directly detect positrons. The IMIC sensors were produced in 5 different configurations. Measurements using a ^{204}Tl source showed that the sensor parameters can be optimized to boost its performance allowing to increase the sensitivity and reduce the average cluster size. In addition, comparisons between sensor configurations show a clear gain provided by the introduction of CMOS process modifications. Finally, the choice of the optimal sensor configuration will depend on the expected *in vivo* conditions.

Keywords: CMOS image sensors, Monolithic active pixel sensors, Particle detection, Beta Probe, Molecular imaging, Neuroimaging

1. Introduction

Performing neuroimaging on awake and freely moving animals could tighten the links between preclinical and clinical studies in neuroscience and even open the door to a powerful association between behavior studies and real time neuroimaging [1, 2], while the anesthesia remains an inherent limit to this day. Previous works have indeed emphasized that anesthetic drugs impact the ability of PET brain imaging to accurately represent the activity of the awake and freely moving rodent's brain [3, 4]. To overcome anesthesia's potential biases on brain processes, approaches have been developed, mainly focusing on micro-PET devices [5, 6, 7, 8]. A complementary approach

consists in using β^+ sensitive implantable microprobes [9]. This kind of device takes advantage of its *in situ* position and good sensitivity to provide images of a radiotracer's distribution in the implanted structures based on a direct detection of positrons. This allows to generate reliable time activity curves based on local measurements and provides precious information about the molecular exchanges in the brain.

Various types of β^+ sensitive microprobes using passive pixels have been developed in the past [10, 11, 12, 13] but had some noticeable drawbacks. Among them, a non-negligible sensitivity to γ-rays as well as a high contribution of background noise. Considering these limitations, Monolithic Active Pixel Sensors (MAPS) appear to provide a powerful approach for such instruments as the amplification and the signal conversion are integrated within the pixel, thus reducing the noise and increasing the sensitivity. Furthermore, the low density of the silicon combined with the limited sensitive thickness allows to significantly reduce the γ-ray sensitivity [9]. Finally, previous studies have shown that such a sensor features low energy dissipation, which makes it compatible with an *in vivo* implantation [14, 15].

This paper describes the physical characterization of IMIC (Imageur Moléculaire Intra Cérébral), a MAPS array developed for rat brain imaging. It is available in five configurations, which differ in terms of active layer thicknesses as well as in the CMOS processes used for their fabrication. These variations were introduced in order to optimize the charge collection and the sensitivity, aiming to improve their overall performances.

2. Material & methods

2.1. IMIC sensor description

2.1.1. General characteristics

The MAPSSIC probe relies on two 610 µm wide, 14700 µm long and 200 µm thick MAPS called IMIC [9, 14, 15]. The pixel front-end is derived from the ALPIDE chip developed for the ALICE experiment at the CERN Large Hadron Collider [16]. The sensitive area contains 16 × 128 pixels of dimensions 30 µm × 50 µm separated in the middle by a 14.73 µm vertical gap accommodating the digital part driving the readout of the pixels. The pixel array is surrounded by a non sensitive silicon area of around 45 µm to 60 µm on the left and right sides and 80 µm at the bottom end of the sensor, enclosed by a guard ring. An approximately 10 µm thick CMOS electronic precedes the epitaxial layer that acts as a particle detector. All pixels use a binary readout (1 bit) of hits passing a globally set energy threshold. The readout of the matrix is done in a rolling shutter manner with an adjustable readout frequency. The integration time can vary from 600 µs to 65 s in the current configuration. A pulse injection capacitor allows to make test charge injections in the input of the front-end's electrodes [16, 17] with an uncertainty of 2.7 % determined by the post-layout simulations. Finally, a backside layer of around 150 µm of silicon substrate ensures the mechanical robustness of the sensors. The resulting MAPSSIC probe is made out of two IMIC sensors that are glued back to back and thus has a thickness of less than 450 µm. This two-sensor assembling allows to double the sensitivity of a given probe while recording an information that is not confined only to 180°. On top of that, it ensures a better mechanical robustness of the probe as it doubles the overall thickness. This paper will not discuss measurements on the two-sensor probe but rather on the single-sensor IMIC.

2.1.2. IMIC configurations

The sensors were designed in five different configurations that vary, in terms of epitaxial layer thicknesses, from 25 µm for the standard sensor (IMIC-a) and 50 µm for some modified ones (IMIC-b). Doubling the epitaxial layer thickness was introduced in order to study the potential gains in sensitivity, especially by increasing the detection efficiency of particles entering the sensitive layer from the lateral edges of the sensors. In addition to the variations in epitaxial layer thicknesses, the sensors also differ due to modifications of the CMOS process used for their fabrication [18]. These variations were introduced in order to maximize the charge collection. The modifications of the CMOS process were also meant to increase the radiation hardness of the MAPS which is relevant for applications in high-energy physics. However, the radiation hardness should not be a limiting factor for neuroimaging applications even in longitudinal studies which consist in repeated measurements to follow particular individuals over prolonged periods of time, as the activities used should be fairly low (around 10 MBq).

The standard CMOS process and the modifications introduced are shown in figure 1 (illustrations derived from [18]). In the standard configuration, the depletion zone is not fully extended laterally in the epitaxial layer between deep p-well and substrate. This effectively creates a gap between pixels that can cause a loss in sensitivity due to a part of charge which will be collected by slow diffusion instead of drift in the depleted region. To overcome this issue, the addition of a deep low-dose n-type implant has been introduced (figures 1.b and 1.c) to help create a full depletion of the epitaxial layer thanks to a planar junction under the collection electrode. This extends the depleted zone over the full pixel area in depth as well as laterally, regardless of the reverse bias used.

Although charges can be created anywhere in the epitaxial layer, their collection depends on the direction and magnitude of the electric field [18]. A uniform and high electric field is indeed a key to avoid charge diffusion that causes charge sharing and would ultimately mean a loss in sensitivity. This is due to the fact that even though the energy lost by a given particle is supposedly higher than the pixel threshold globally set, if charge sharing occurs, the amount of charge collected by each pixel electrode may fall below the threshold. As a result, no pixel is activated despite the energy initially deposited being enough to trigger a detection. This is particularly problematic as the energy range of incoming positrons is continuous. As showed in a previous Monte Carlo study on a sensor with the same architecture and comparable sensitive layer thickness [9], the energy loss spectrum for ^{18}F is expected to be up to 100 keV with a most probable energy loss being below 7 keV. In such a sensor, the interaction of a particle in the sensitive layer usually leads to the activation of not one but a group of pixels called cluster (figure 1.d). The number of activated pixels and therefore the size of the clusters is greatly influenced by the electric field. For instance, a weak electric field will induce the activation of more pixels for a given recorded event resulting in larger clusters. This will make the event identification more difficult and error prone at high count rates due to pile-up, with the binary readout on 1 bit used to satisfy space constraints and to limit the power consumption down to 55 nW/pixel according to simulations [14]. At high count rate, there can be an accumulation of counts on pixels that have already been activated during the integration. Because of the binary readout, such pixels cannot give

information about additional events thus complicating the identification of events. The pile-up probability increases with the size of the clusters.

A major contributing factor to the charge sharing for sensors using a small collection electrode, such as IMIC, is the non-uniformity of the electric fields [18, 19], dropping to a minimum value at the pixel corners close to the aforementioned deep planar junction. This is due to a weak lateral electric field compared to the potential difference between the N-implant and the backside P-substrate. Figures 1.b and 1.c show two different approaches to increase the lateral electric field at the pixel borders: the process modification #2 (figure 1.b) involves the creation of a gap in the deep n-implant while the process modification #3 (figure 1.c), introduces an additional deeply buried p-type implant (deep p-well) at the pixel border. These modifications in the CMOS process aim to ensure a better drive of the charges towards the collection electrodes, reducing the drift path and the charge sharing. The first three rows of table 1 reference the five IMIC configurations and their respective characteristics.

2.2. Measurements

All measurements were performed on single IMIC sensors in a light shielding and constant climate chamber. A setup was built in order to perform measurements using a sealed radioactive source in the same conditions regardless of the studied IMIC configuration. It was composed of a test PCB to which the single sensor was connected. A source holder was then fixed on the PCB in order to set an invariant position of the source providing a uniform irradiation of the sensors (figure 2) as all PCBs and source holders used were identical to the sub-milimeter. The IMIC sensors were mechanically placed in the same position on each PCB. The source was placed in the same position and could not move around or rotate as it was tightly fixed. Finally, the 3 mm active diameter of the source considerably reduces the effect of any sub-milimetric variation in the set up positions. The temperature of the setup was fixed to 38.5°C, as it is the maximum brain temperature expected for rats [20] when stimulated.

2.2.1. Parameter settings

The pixel front-end biasing currents and voltages are provided by 14 internal programmable DACs and are common for all pixels in the array. Before operating the sensor, the correct range of biasing signals needed to be determined. For that, post layout electrical simulations allowed to have nominal values for all parameters. These values were set separately for each IMIC configuration and reverse bias as they affect the operating points of the front end. The parameter that regulates the energy loss threshold [21], was fine tuned around the initial value provided by simulations. The energy loss threshold, which will be referred to as "energy threshold" for simplicity, is the energy that needs to be deposited in a pixel to trigger its activation with a probability of 50 %. The tuning was done using injections of about 350 electrons into the pixels using the internal injection system, while varying the parameter value, thus, the energy thresholds. This allowed, for a given configuration and reverse bias voltage, to determine a range of achievable energy thresholds with which the sensor is able to correctly respond to such injections. The range includes a minimum threshold for noise-free operation as well as a maximum threshold set

between 1 keV to 1.5 keV which corresponds to our goal in order to maximize the overall sensitivity as well as the β^+/γ sensitivity ratio. A second phase consisted of a series of noise measurements without any radiation source in this range of energy thresholds for background determination. As the energy threshold level has a big influence for the pixel activation, it was the subject of a deep study. Therefore, the performances of each IMIC were compared using several energy threshold values chosen within the range of achievable thresholds determined previously. This allowed to study if this crucial parameter can be optimized to maximize the sensor's performance.

2.2.2. Background

The background noise was measured as the number of clusters activated during multiple hours of integration without any source of radiation for each IMIC configuration. These measurements were performed using no reverse bias (reverse bias of 0 V) and the lowest threshold achievable.

2.2.3. Threshold

In order to determine the average energy threshold value of the sensor, a variable amount of charges was injected to the front-end of 10 % of the pixels [22], applying reverse bias voltages from 0 V to 2 V to the substrate. The process was repeated 10 times for every pixel injected. The energy threshold E_{thr} was determined as the charge, that induces a pixel activation with a probability of 50 % as from the s-curve on each pixel's activation probability using a logistic regression method. In order to use a unit that is more indicative for the use of the probe, the deposited charge is converted to absorbed energy, considering 3.67 eV are needed to create an electron-hole pair in silicon at room temperature [23]. Additionally, the average individual pixel equivalent noise charge (ENC) was determined for each IMIC, energy threshold and reverse bias.

2.2.4. Performance measurements

A short integration time of 1 ms was chosen to limit the number of events recorded in each frame in order to minimize the pile-up probability.

Source measurements for a comparative study between different IMIC configurations were performed using a sealed ^{204}Tl source (whose energy spectrum is close to ^{18}F positron one: β^-, maximum energy: 0.764 MeV) of 3 mm active diameter placed at a distance of 14.3 mm from the probe. The influence of both the threshold and the reverse bias on the sensors' performance was studied since these two parameters are of great importance in the MAPS technology. To assess these performances, particular attention was paid to two crucial metrics: the sensitivity and the average cluster size. In this paper, the count rate (defined as the number of activated clusters) is used as an observable that scales with the sensitivity.

3. Results

3.1. Background

Table 1 shows the result of the background measurements, in clusters per second, for all types of IMIC with the lowest threshold setting available. All sensor configurations display a low background noise recording less than 10×10^{-3} cps.

3.2. Threshold

Figure 3 shows the mean activation probability as a function of the injected charge for IMIC-1a at 0 V. The chart also displays the corresponding histogram of the individual pixel-threshold distribution. A Poissonian distribution is noticeable with only a handful of pixels having a slightly higher energy threshold. Table 2 shows the threshold range for each IMIC configuration. For all sensor configurations, the energy threshold is under 1.2 keV. The threshold level gradually decreases when a higher reverse bias is applied for IMIC-1a. However, for all sensors with a modified CMOS process, the increase of the reverse bias systematically induces an increase of the energy threshold level. The standard deviation of the individual pixel-threshold histogram for each sensor varies for all IMIC configurations from around 30 eV to 100 eV and is displayed in table 2.

Table 2 displays the average ENC for each IMIC and figure 4 shows it for IMIC-1a versus energy threshold. For all sensors the ENC decreases as the energy threshold increases. No clear trend is observed when studying the influence of the reverse bias on the ENC even though at low threshold, a 2 V reverse bias induces an increase of around 12 % of the ENC.

3.3. Performance measurement

3.3.1. Energy threshold influence

Figure 5 shows the variation of the sensitivity and cluster size with the energy threshold for IMIC-1a at three reverse biases. As shown by the fits, the sensitivity appears to decrease linearly with the threshold. A lower threshold level has a slight and linear impact on the IMIC-1a sensor sensitivity inducing at best a 3.1 % increase in sensitivity compared with the highest threshold value available. The same goes for IMIC-2b, IMIC-3a and 3b for which a decrease in the threshold value permits an increase of the sensitivity by up to 5 %, 2 % and 2 %, respectively. Finally, IMIC-2a appears to have a more stable sensitivity response across its range of energy threshold values with an increase of less than 1 % at low threshold. Figure 6 shows indeed a very different impact of the threshold on the sensitivity between IMIC-1a and IMIC-2a. Despite the noted gain in sensitivity, the performance of the sensors in terms of cluster size are more altered by the decrease of the threshold. The average cluster size exponentially increases as the threshold value gets lower with a drop of 19 % to 33 % for IMIC-1a, 13 % for IMIC-2a, 11 % to 14 % for IMIC-2b, 8 % for IMIC-3a and 12 % to 15 % for IMIC-3b. The dependency of the cluster size on the energy threshold is also illustrated in figure 6 showing the variation in the distribution of the cluster size at three energy threshold levels for IMIC-1a and IMIC-2a. The increase of the threshold has indeed more impact for IMIC-1a as it helps suppressing an important part of charges collected through diffusion whereas IMIC-2b mainly relies on charge drift even at low threshold thanks to an optimized electric field.

3.3.2. Reverse bias influence

Variations in performances are shown in figure 5 for the standard IMIC configuration (IMIC-1a). The increase of the reverse bias induces an increase in sensitivity. For instance, while a reverse bias of 1 V allows a marginal gain compared to the 0 V bias (around 1 % on average across the threshold range), the gain in sensitivity at 2 V is

greater (4 % going from 1 V to 2 V). This increase in sensitivity is also followed by a decrease of 24 % in the average cluster size. However, when studying other sensor configurations (Table 2), while the same behavior is observed in terms of average cluster size reduction, no clear gain in sensitivity is induced by an increased reverse bias. For IMIC-2b and IMIC-3b for instance, a slight drop in sensitivity of 4 % and 3 %, respectively is noted for the lowest threshold configuration. For all IMIC configurations, an increase of the reverse bias provides better performances in terms of cluster size (table 2), hence reducing the pile-up probability. At 2 V, the IMIC-1a shows a reduction of 22 % compared to 0 V bias and 13 % to 1 V, respectively. Furthermore, the IMIC-2a displays a cluster size reduction of 4 % on average using a 1 V reverse bias while the IMIC-2b allows a maximum cluster size decrease of around 10 %. Finally, IMIC-3a allows to reduce the average cluster size by 13 % at best, and IMIC-3b enables a 9 % reduction.

3.3.3. IMIC sensor comparison

Table 2 shows the variations in sensitivity and cluster size for various energy thresholds and reverse bias values for each IMIC configuration.

An increase in sensitivity up to 7 % is seen for sensors with modified CMOS process and a 25 µm epitaxial layer (IMIC-2a and IMIC-3a) and up to 12 % for sensors with a 50 µm epitaxial layer (IMIC-2b and IMIC-3b) compared to the IMIC-1a. Additionally, changes of the threshold value tend to have a greater impact on the sensitivity for IMIC-1a compared to the others as shown by the color map in figure 6. The best performances in terms of average cluster size are achieved with modified sensors having a 25 µm epitaxial layer (IMIC 2a and IMIC 3a) thanks to a reduced drift path and an optimized charge collection. Figure 6 shows the distribution of the cluster size for IMIC-1a and IMIC-2a, which induce respectively the largest and the smallest cluster sizes on average. A clear difference is observed as IMIC-1a displays a wider distribution of cluster size while IMIC-2a provides a narrower one, with a majority of clusters composed of one to two pixels. The increase of the energy threshold allows to significantly reduce the cluster size for IMIC-1a and get closer to the performances achieved by IMIC-2a, which is less affected by such a change. IMIC-2a and IMIC-3a allow for a reduction of 51 % to 64 % of the average cluster size, limiting considerably the pile-up probability. Although sensors with a 50 µm epitaxial layer have smaller clusters on average than IMIC-1a (reduction of 20 % to 28 % at best), they still show larger clusters compared to IMIC-2a and 3a due to the longer path needed for the collection of the charges as they can be created deeper in the epitaxial layer, thus facilitating charge sharing between pixels.

Finally, the minimal energy threshold achieved for each IMIC configuration seems to have a little impact on the differences seen between sensors both in terms of sensitivity and cluster size as shown by table 2. IMIC-1a has the lowest sensitivity of all sensors despite displaying the lower energy threshold regardless of the reverse bias. On the other hand, IMIC-3b provides by far the highest sensitivity despite having among the highest minimal energy threshold both at 0 V and 1 V. The results show that the impact of the minimal energy threshold on the sensitivity is outweighed by other contributing factors such as the CMOS process or the epitaxial layer thickness.

The same observation can be made about the cluster size as IMIC-2b and IMIC-3b induce significantly larger clusters compared to IMIC-2a and IMIC-3a respectively which have the same CMOS processes and similar thresholds but thinner epitaxial layers.

4. Discussion

Given that in *in vivo* conditions, the signal is expected to be around few events per seconds in pharmacological studies to approximately a hundred events per seconds in physiological studies [9], the background noise exhibited by all the configurations of IMIC, being 3 to 5 orders of magnitude smaller, is considered to be acceptable.

The energy threshold study that was carried out confirms that the parameters set up for IMIC sensors are in good agreement with a low energy threshold goal well below 1.5 keV per pixel. The ENC is higher than the one measured in previous studies [17] though it is still one order of magnitude smaller than the thresholds actually measured. The ENC decreases as the energy threshold increases. Furthermore, for IMIC-1a, results from source measurements show that the higher the reverse bias, the better the performances, hence insuring a maximization of the sensitivity and a limitation of the pile-up probability. On the other hand, no gain in sensitivity is noted for increased reverse bias on sensors with a modified CMOS process. This can be due to an increase in the average energy threshold when biasing these sensors with 1 V. This change in the average energy threshold value either mitigates (IMIC 2a and 3a) and even outweighs (IMIC 2b and 3b) the gain provided by the better charge collection at 1 V resulting in a stagnating or dropping sensitivity. This shows that the charge collection is the main factor of improvement when the reverse bias is increased. Furthermore, as the charge collection is dominated by the charge drift for sensors with a modified CMOS process, the increase of the reverse bias only marginally improves the charge collection as it is already optimized. On the other hand, standard sensors greatly benefit from an increased reverse bias as it limits the charge diffusion and favors the drift. Finally, previous studies have shown that the reverse bias should be higher (up to 6 V) to provide bigger gains in sensitivity [24]. This is also confirmed by the notable gain provided by the use of a 2 V reverse bias with the IMIC-1a. However, for reverse biases from 2 V to 6 V, it was not possible to determine a range of suitable pixel parameters with the modified CMOS process IMIC sensors. This issue is currently under study. Nevertheless, the increase of the reverse bias has a positive effect on the average cluster size for all tested reverse-bias voltages, which is also shown in previous studies [25].

Results both in terms of sensitivity and average cluster size show improved performances with the modified sensors compared to the standard IMIC-1a. Despite a unique sensor geometry, these results are in agreement with previous studies [18, 24, 26] carried out on sensors used for high energy particle detection. The aforementioned studies show similar gains with modified CMOS processes demonstrating significantly better performances than the standard ones, especially at low reverse biases (0 V). These performances are caused by a fully depleted epitaxial layer as well as a better charge collection based on charge drift and the limitation of slow diffusion. However, in contrast to the cited studies, a slight difference in performances between sensors with the modified CMOS processes

#2 and #3 can be noted. Sensors with the modified CMOS process #2 (IMIC 2a and 2b) show indeed a lower sensitivity and a slightly smaller cluster size on average compared to the modified CMOS process #3 (IMIC 3a and 3b) despite slightly lower energy thresholds. These comparative measurements show that choosing the best suited IMIC configuration will depend on the expected *in vivo* conditions. For instance, if a low count rate is expected, one should rather rely on 50 µm epitaxial layer sensors such as IMIC-2b and IMIC-3b as these will help maximizing the sensitivity. This should particularly be the case in pharmacological studies [27]. As shown in a previous study, having a 50 µm epitaxial layer will only marginally increase the proportion of gamma rays to the total sensitivity by less than 3 % [9]. On the other hand, if the count rate is expected to be high, like in physiological studies for instance, IMIC-2a and IMIC-3a appear to be better alternatives as they will notably limit the pile-up probability. The same trade-off arises when trying to optimize the energy threshold as a low threshold will increase both the sensitivity and the cluster size and, consequently, the pile-up probability.

Conclusion

A new version of IMIC, a monolithic active pixel sensor was produced in five different configurations. Measurements performed with a sealed β^- radioactive source as well as charge injections have shown that such a sensor is capable of recording a signal based on the detection of low energy charged particles. Optimization of the aforementioned detection proved to be possible through a trade-off between increased sensitivity and limited pile-up probability. Furthermore, the experimental validation carried out have also allowed to validate the gains in performances induced by modifications in the CMOS process.

Acknowledgment

This project has received financial support from the CNRS through the MITI interdisciplinary programs.

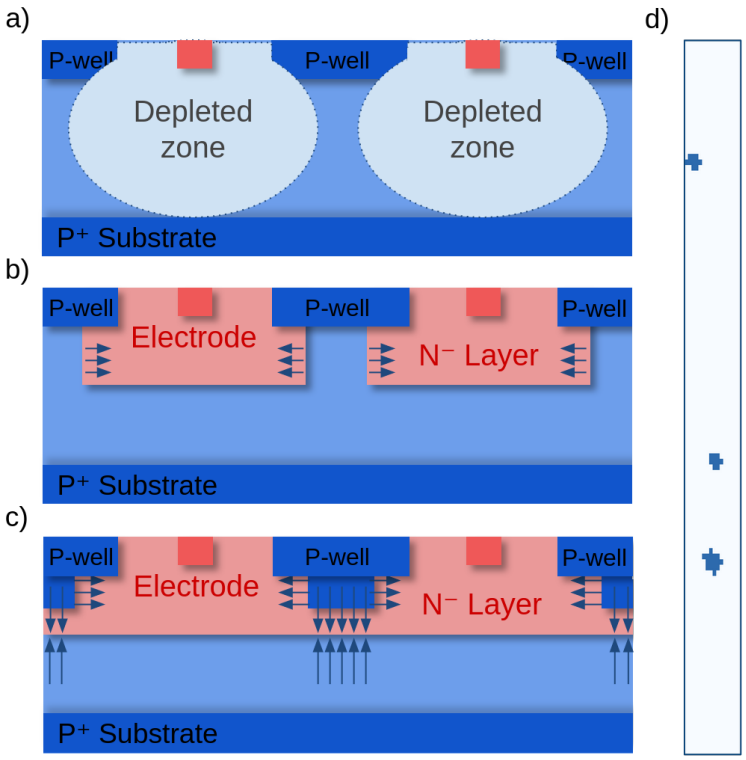

Figure 1: Schematic cross section (not to scale) of three CMOS processes with a small collection electrode. a) Standard CMOS process, b) Modified CMOS process #2 with a gap in the deep n-implant, c) Modified CMOS process #3 with an additional deeply buried p-type implant (deep p-well). The arrows show the electric field lines around the gap/p-type implants. d) Single frame composed of 128 × 16 pixels clearly showing three different clusters resulting from the interaction of β^- particles from a ^{204}Tl source.

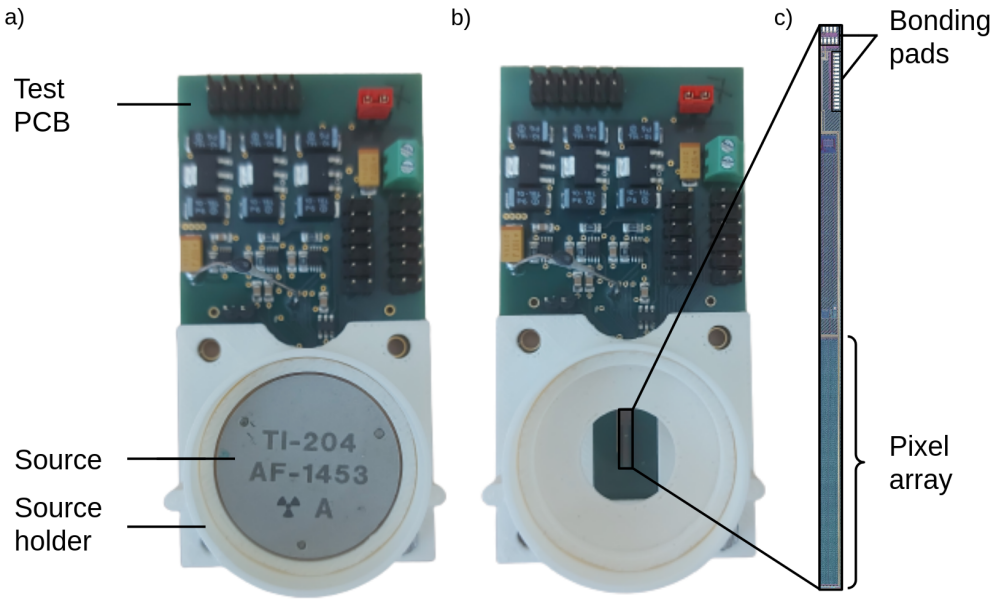

Figure 2: Pictures of the experimental setup for measurements with a sealed source. a) Test PCB mounted with the source holder and a ^{204}Tl source in place. b) Test PCB mounted with the source holder with no source in place showing the IMIC. c) Picture of the IMIC showing the pixel array and the bonding pads.

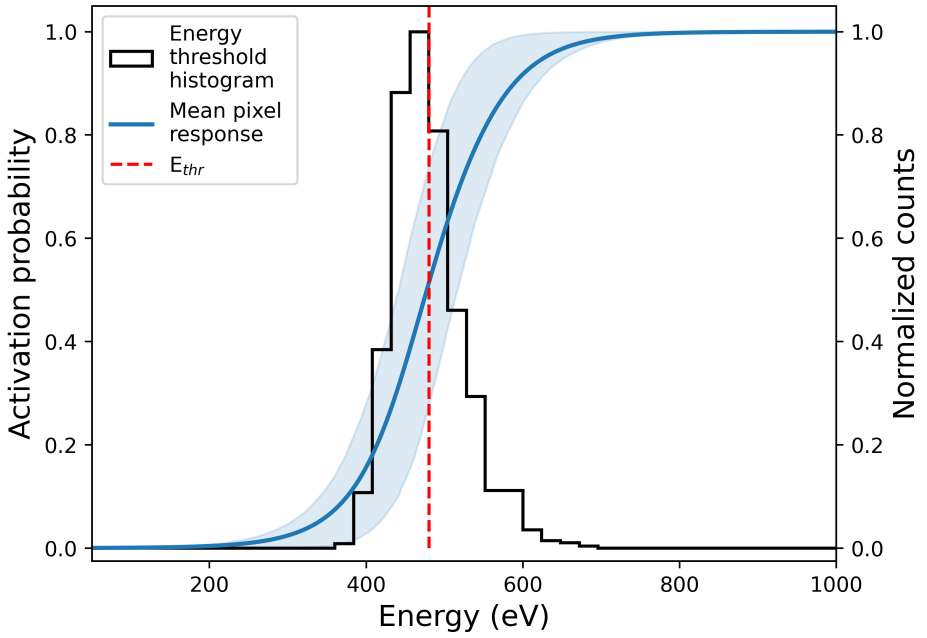

Figure 3: Blue line: Average pixel activation probability as a function of the injected charge for IMIC-1a associated with the 16^{th} and 84^{th} quantiles (light blue). Bars: individual pixel energy threshold distribution for all the 2048 pixels of the IMIC 1-a. Dotted red line: Average energy threshold of the IMIC-1a for the given set of parameters.

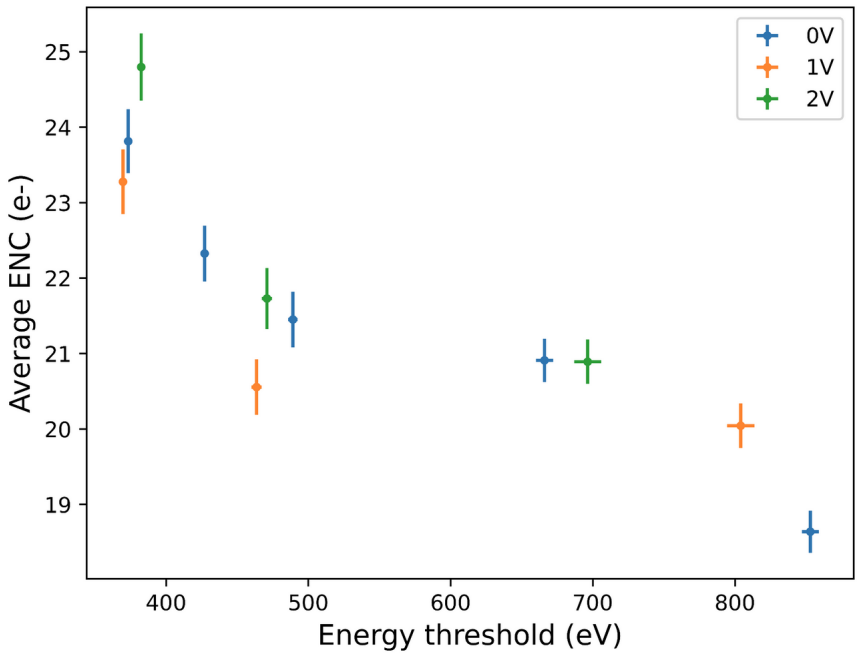

Figure 4: Average ENC as a function of the energy threshold for IMIC-1a at 3 reverse biases. Uncertainty bars are the propagated uncertainties on absolute value of charge injection.

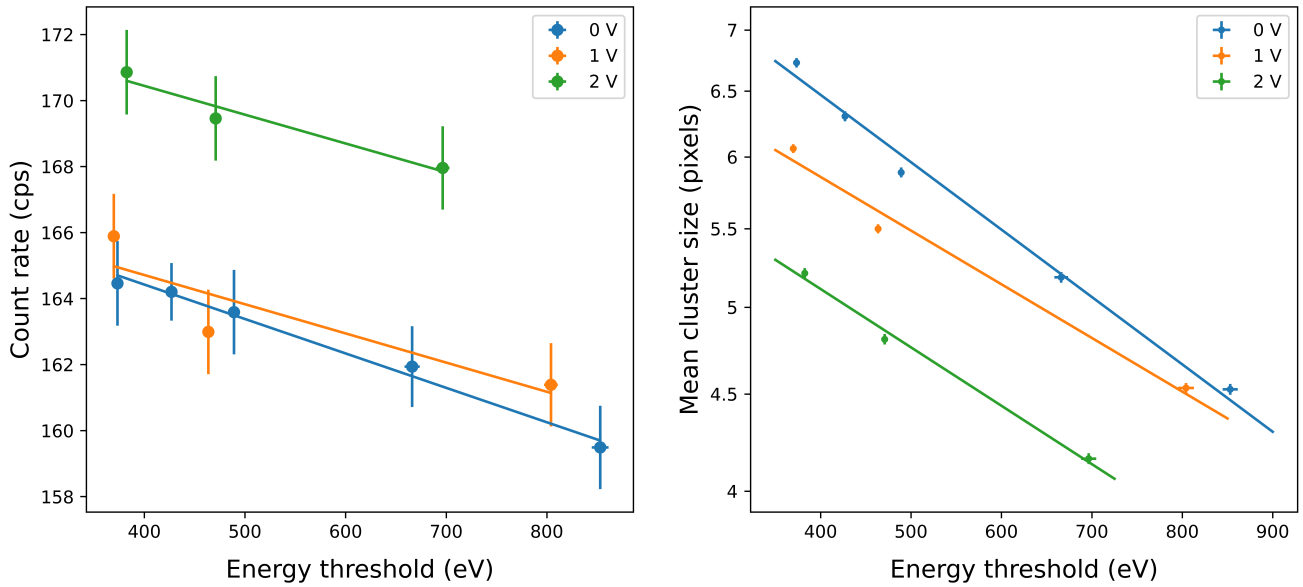

Figure 5: Left: Sensitivity as a function of the energy threshold for IMIC-1a at 3 reverse biases. Uncertainty bars showing the standard deviation assuming a Poissonian distribution. Lines show a linear fit corresponding to the data. Right: Average cluster size as a function of the energy threshold for IMIC-1a at 3 reverse biases (in logarithmic scale). Uncertainty bars show the standard deviation on the mean. Lines show the exponential fits corresponding to the data.

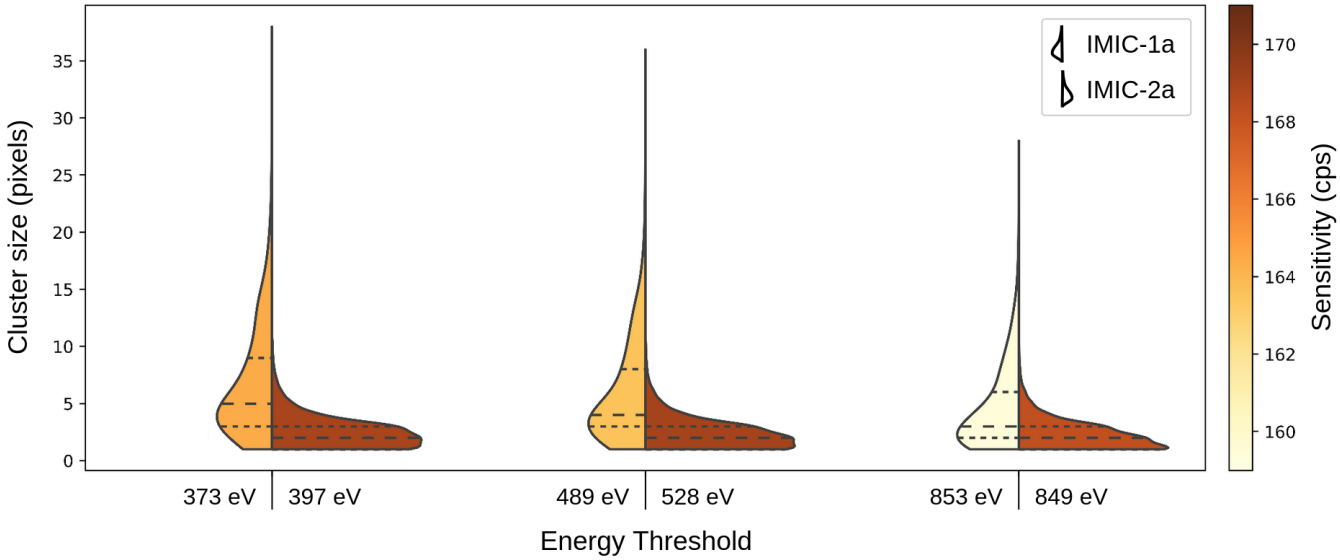

Figure 6: Violin plot showing the distribution of the cluster size at three energy thresholds for IMIC-1a (left semi-violins) and IMIC-2a (right semi-violins). For each distribution (semi-violins), the lower and the upper short dashed lines represent the first and third quartile respectively and the long dashed line in between represents the median. For the IMIC-2a, (right semi-violins) the first quartile is so low that it is actually confounded with the edge of the distribution. The color palette shows the variation of the sensitivity for these threshold values.

IMIC Configuration	**1a**	**2a**	**2b**	**3a**	**3b**
CMOS process	Standard	Gap (#2)	Gap (#2)	Deep p-well (#3)	Deep p-well (#3)
Epitaxial layer thickness (µm)	25	25	50	25	50
Background ($\times$ 10^{-3} cps)	1.09 ± 0.10	1.70 ± 0.47	4.30 ± 0.66	2.10 ± 0.46	7.50 ± 0.87

Table 1: Detailed characteristics and background noise count rate in counts (clusters) per second per sensor for each IMIC configurations.

IMIC Config.	**Reverse bias**	**Energy threshold range (eV)**	**Energy threshold std dev. (eV)**	**Average ENC (e^-)**	**Mean count rate (cps)**	**Average cluster size (pixels)**
1a	0 V	853 ± 6 - 373 ± 3	82 - 36	19 - 24	159.5 - 164.5	4.5 - 6.7
	1 V	804 ± 7 - 370 ± 3	97 - 36	20 - 23	161.4 - 165.9	4.5 - 6.1
	2 V	696 ± 7 - 382 ± 3	96 - 36	21 - 25	168.0 - 170.9	4.2 - 5.2
2a	0 V	849 ± 7 - 397 ± 3	101 - 45	18 - 25	168.2 - 168.9	2.2 - 2.4
	1 V	1037 ± 5 - 514 ± 4	70 - 52	15 - 22	168.7 - 168.5	2.1 - 2.4
2b	0 V	960 ± 5 - 531 ± 4	74 - 51	16 - 21	170.5 - 174.1	4.2 - 4.93
	1 V	1176 ± 4 - 665 ± 6	59 - 79	20 - 32	164.1 - 171.6	3.9 - 4.4
3a	0 V	1077 ± 4 - 670 ± 6	57 - 90	16 - 33	170.8 - 174.1	2.3 - 2.5
	1 V	1212 ± 4 - 1167 ± 4	57 - 62	15 - 15	172.4 - 175.0	2.2 - 2.2
3b	0 V	1028 ± 5 - 546 ± 5	76 - 68	16 - 23	178.4 - 178.6	4.6 - 5.4
	1 V	1226 ± 6 - 856 ± 7	85 - 103	20 - 21	172.3 - 174.9	4.3 - 4.9

Table 2: Table of the performances in terms of sensitivity and cluster size using a ^{204}Tl sealed source as a function of the threshold and reverse bias used for all the IMIC configurations. The sensitivity and cluster size values presented correspond to the lowest and highest values of the achievable energy thresholds.

References

[1] I. Yalcin, F. Barthas, M. Barrot, Emotional consequences of neuropathic pain: Insight from preclinical studies, Neuroscience & Biobehavioral Reviews 47 (2014) 154–164. https://doi.org/10.1016/j.neubiorev.2014.08.002.

[2] Y.-R. Gao, Y. Ma, Q. Zhang, A.T. Winder, Z. Liang, L. Antinori, P.J. Drew, N. Zhang, Time to wake up: Studying neurovascular coupling and brain-wide circuit function in the un-anesthetized animal, NeuroImage 153 (2017) 382–398. https://doi.org/10.1016/j.neuroimage.2016.11.069.

[3] A.K.O. Alstrup, D.F. Smith, Anaesthesia for positron emission tomography scanning of animal brains, Lab Anim 47 (2013) 12–18. https://doi.org/10.1258/la.2012.011173.

[4] V.D. Patel, D.E. Lee, D.L. Alexoff, S.L. Dewey, W.K. Schiffer, Imaging dopamine release with Positron Emission Tomography (PET) and 11C-raclopride in freely moving animals, NeuroImage 41 (2008) 1051–1066. https://doi.org/10.1016/j.neuroimage.2008.02.065.

[5] D. Schulz, S. Southekal, S.S. Junnarkar, J.-F. Pratte, M.L. Purschke, S.P. Stoll, B. Ravindranath, S.H. Maramraju, S. Krishnamoorthy, F.A. Henn, P. O'Connor, C.L. Woody, D.J. Schlyer, P. Vaska, Simultaneous assessment of rodent behavior and neurochemistry using a miniature positron emission tomograph, Nat Methods 8 (2011) 347–352. https://doi.org/10.1038/nmeth.1582.

[6] H. Takuwa, J. Maeda, Y. Ikoma, M. Tokunaga, H. Wakizaka, S. Uchida, I. Kanno, J. Taniguchi, H. Ito, M. Higuchi, [11 C]Raclopride binding in the striatum of minimally restrained and free-walking awake mice in a positron emission tomography study: FREE-WALKING AWAKE-MOUSE PET SYSTEM, Synapse 69 (2015) 600–606. https://doi.org/10.1002/syn.21864.

[7] A.Z. Kyme, V.W. Zhou, S.R. Meikle, R.R. Fulton, Real-time 3D motion tracking for small animal brain PET, Phys. Med. Biol. 53 (2008) 2651–2666. https://doi.org/10.1088/0031-9155/53/10/014.

[8] M.G. Spangler-Bickell, B. De Laat, R. Fulton, G. Bormans, J. Nuyts, The effect of isoflurane on 18F-FDG uptake in the rat brain: a fully conscious dynamic PET study using motion compensation, EJNMMI Res 6 (2016) 86. https://doi.org/10.1186/s13550-016-0242-3.

[9] L. Ammour, J. Heymes, M. Bautista, S. Fieux, F. Gensolen, M. Kachel, A. Dubois, F. Lefebvre, F. Pain, P. Pangaud, L. Pinot, J. Baudot, P. Gisquet-Verrier, P. Laniece, C. Morel, L. Zimmer, M.-A. Verdier, MAPSSIC, a Novel CMOS Intracerebral Positrons Probe for Deep Brain Imaging in Awake and Freely Moving Rats: A Monte Carlo Study, IEEE Trans. Radiat. Plasma Med. Sci. 3 (2019) 302–314. https://doi.org/10.1109/TRPMS.2018.2881301.

[10] L. Balasse, J. Maerk, F. Pain, A. Genoux, S. Fieux, F. Lefebvre, C. Morel, P. Gisquet-Verrier, P. Lanièce, L. Zimmer, PIXSIC: A Wireless Intracerebral Radiosensitive Probe in Freely Moving Rats, Mol Imaging 14 (2015) 7290.2015.00020. https://doi.org/10.2310/7290.2015.00020.

[11] J. Märk, D. Benoit, L. Balasse, M. Benoit, J.C. Clémens, S. Fieux, D. Fougeron, J. Graber-Bolis, B. Janvier, M. Jevaud, A. Genoux, P. Gisquet-Verrier, M. Menouni, F. Pain, L. Pinot, C. Tourvielle, L. Zimmer, C. Morel, P. Laniece, A wireless beta-microprobe based on pixelated silicon for in vivo brain studies in freely moving rats, Phys. Med. Biol. 58 (2013) 4483–4500. https://doi.org/10.1088/0031-9155/58/13/4483.

[12] M. Benoit, J. Märk, P. Weiss, D. Benoit, J.C. Clemens, D. Fougeron, B. Janvier, M. Jevaud, S. Karkar, M. Menouni, F. Pain, L. Pinot, C. Morel, P. Laniece, New concept of a submillimetric pixellated Silicon detector for intracerebral application, Nuclear Instruments and Methods in Physics Research Section A: Accelerators, Spectrometers, Detectors and Associated Equipment 659 (2011) 499–503. https://doi.org/10.1016/j.nima.2011.08.027.

[13] P. Millet, M.M. Sallanon, J.-M. Petit, Y. Charnay, P. Vallet, C. Morel, R. Cespuglio, P.J. Magistretti, V. Ibáñez, In Vivo Measurement of Glucose Utilization in Rats using a β-Microprobe: Direct Comparison with Autoradiography, J Cereb Blood Flow Metab 24 (2004) 1015–1024. https://doi.org/10.1097/01.WCB.0000129416.72638.94.

[14] J. Heymes, L. Ammour, M. Bautista, G. Bertolone, A. Dorokhov, S. Fieux, F. Gensolen, M. Goffe, F. Guezzi-Messaoud, C. Hu-guo, M. Kachel, F. Lefebvre, F. Pain, P. Pangaud, L. Pinot, M. Winter, P. Gisquet-Verrier, P. Laniece, C. Morel, M.-A. Verdier, L. Zimmer, J. Baudot, IMIC — needle-shaped low-power monolithic active pixel sensor for molecular neuroimaging on awake and freely moving rats, in: 2016 IEEE Nuclear Science Symposium, Medical Imaging Conference and Room-Temperature Semiconductor Detector Workshop (NSS/MIC/RTSD), IEEE, Strasbourg, 2016: pp. 1–4. https://doi.org/10.1109/NSSMIC.2016.8069414.

[15] F. Gensolen, L. Ammour, M. Bautista, J. Heymes, S. Fieux, M. Kachel, F. Lefebvre, P. Pangaud, L. Pinot, P. Lanièce, J. Baudot, P. Gisquet, L. Zimmer, M.-A. Verdier, C. Morel, MAPSSIC, a communicating MAPS-based intracerebral positrons probe for deep brain imaging in awake and freely-moving rats, EPJ Web Conf. 225 (2020) 09002. https://doi.org/10.1051/epjconf/202022509002.

[16] G. Aglieri Rinella, The ALPIDE pixel sensor chip for the upgrade of the ALICE Inner Tracking System, Nuclear Instruments and Methods in Physics Research Section A: Accelerators, Spectrometers, Detectors and Associated Equipment 845 (2017) 583–587. https://doi.org/10.1016/j.nima.2016.05.016.

[17] C. Yang, C. Feng, J. Liu, Y. Teng, S. Liu, Q. An, X. Sun, P. Yang, A Prototype Readout System for the ALPIDE Pixel Sensor, IEEE Trans. Nucl. Sci. 66 (2019) 1088–1094. https://doi.org/10.1109/TNS.2019.2913335.

[18] M. Munker, M. Benoit, D. Dannheim, A. Fenigstein, T. Kugathasan, T. Leitner, H. Pernegger, P. Riedler, W. Snoeys, Simulations of CMOS pixel sensors with a small collection electrode, improved for a faster charge collection and increased radiation tolerance, J. Inst. 14 (2019) C05013–C05013. https://doi.org/10.1088/1748-0221/14/05/C05013.

[19] D. Dannheim, A. Fiergolski, J. van Hoorne, D. Hynds, W. Klempt, T. Kugathasan, M. Munker, A. Nürnberg, K. Sielewicz, W. Snoeys, S. Spannagel, Comparison of small collection electrode CMOS pixel sensors with partial and full lateral depletion of the high-resistivity epitaxial layer, Nuclear Instruments and Methods in Physics Research Section A: Accelerators, Spectrometers, Detectors and Associated Equipment 927 (2019) 187–193. https://doi.org/10.1016/j.nima.2019.02.049.

[20] E. Briese, Normal body temperature of rats: the setpoint controversy, Neuroscience & Biobehavioral Reviews 22 (1998) 427–436. https://doi.org/10.1016/S0149-7634(97)00051-1.

[21] G. Aglieri, C. Cavicchioli, P.L. Chalmet, N. Chanlek, A. Collu, P. Giubilato, H. Hillemanns, A. Junique, M. Keil, D. Kim, J. Kim, T. Kugathasan, A. Lattuca, M. Mager, C.A.M. Tobon, D. Marras, P. Martinengo, S. Mattiazzo, G. Mazza, H. Mugnier, L. Musa, D. Pantano, C. Puggioni, J. Rousset, F. Reidt, P. Riedler, S. Siddhanta, W. Snoeys, G. Usai, J.W.V. Hoorne, P. Yang, J. Yi, Monolithic active pixel sensor development for the upgrade of the ALICE inner tracking system, J. Inst. 8 (2013) C12041–C12041. https://doi.org/10.1088/1748-0221/8/12/C12041.

[22] V. Raskina, F. Křížek, Characterization of Highly Irradiated ALPIDE Silicon Sensors, Universe 5 (2019) 91. https://doi.org/10.3390/universe5040091.

[23] K.A. Olive, Review of Particle Physics, Chinese Phys. C 38 (2014) 090001. https://doi.org/10.1088/1674-1137/38/9/090001.

[24] I. Berdalovic, R. Bates, C. Buttar, R. Cardella, N.E. Plaja, T. Hemperek, B. Hiti, J.W.V. Hoorne, T. Kugathasan, I. Mandic, D. Maneuski, C.A.M. Tobon, K. Moustakas, L. Musa, H. Pernegger, P. Riedler, C. Riegel, D. Schaefer, E.J. Schioppa, A. Sharma, W. Snoeys, C.S. Sanchez, T. Wang, N. Wermes, Monolithic pixel development in TowerJazz 180 nm CMOS for the outer pixel layers in the ATLAS experiment, J. Inst. 13 (2018) C01023–C01023. https://doi.org/10.1088/1748-0221/13/01/C01023.

[25] M. Deveaux, Recent results from the MIMOSIS-1 CMOS MAPS, PSD13 : The 13th International Conference on Position Sensitive Detectors. 3-8 September 2023

[26] K. Dort, R. Ballabriga, J. Braach, E. Buschmann, M. Campbell, D. Dannheim, L. Huth, I. Kremastiotis, J. Kröger, L. Linssen, M. Munker, W. Snoeys, S. Spannagel, P. Švihra, T. Vanat, Comparison of different sensor thicknesses and substrate materials for the monolithic small collection-electrode technology demonstrator CLICTD, (2022). http://arxiv.org/abs/2204.10569 (accessed July 4, 2022).

[27] M.-P. Kung, H.F. Kung, Mass effect of injected dose in small rodent imaging by SPECT and PET, Nuclear Medicine and Biology 32 (2005) 673–678. https://doi.org/10.1016/j.nucmedbio.2005.04.002.